OPEN

Correspondence and
requests for materials
should be addressed to
H.Z.Z. (hozhang@tcd.
ie)

High throughput secondary electron imaging of organic residues on a graphene surface

Yangbo Zhou, Robert O'Connell, Pierce Maguire & Hongzhou Zhang

School of Physics and Centre for Research on Adaptive Nanostructures and Nanodevices (CRANN), Trinity College Dublin, Dublin 2, Ireland.

Surface organic residues inhibit the extraordinary electronic properties of graphene, hindering the development of graphene electronics. However, fundamental understanding of the residue morphology is still absent due to a lack of high-throughput and high-resolution surface characterization methods. Here, we demonstrate that secondary electron (SE) imaging in the scanning electron microscope (SEM) and helium ion microscope (HIM) can provide sub-nanometer information of a graphene surface and reveal the morphology of surface contaminants. Nanoscale polymethyl methacrylate (PMMA) residues are visible in the SE imaging, but their contrast, i.e. the apparent lateral dimension, varies with the imaging conditions. We have demonstrated a quantitative approach to readily obtain the physical size of the surface features regardless of the contrast variation. The fidelity of SE imaging is ultimately determined by the probe size of the primary beam. HIM is thus evaluated to be a superior SE imaging technique in terms of surface sensitivity and image fidelity. A highly efficient method to reveal the residues on a graphene surface has therefore been established.

G raphene is a single sheet of two-dimensional material composed of hexagonally-arranged sp^2 carbon atoms[1]. For the past decade, a vast amount of research has been conducted to understand graphene's characteristics, exemplified by its high carrier mobility[2,3], and to establish its applications, such as graphene terahertz plasmon oscillators[4]. To investigate the properties of graphene, especially its functions in high-performance electronics, pristine graphene needs to be formed, manipulated and fabricated into a myriad of device structures ranging from the micrometer to the nanometer-scale. The process of such device fabrication normally involves several organic chemicals, for instance, polymer photoresists in electron beam lithography. This fabrication technique is known to introduce foreign species to the graphene lattice or to its surface as contaminants, which may adversely alter the intrinsic properties of graphene[5,6]. In many research papers, it is presumed that the presence and effect of residual chemicals (e.g. polymers introduced during the graphene transfer process) can be reduced by annealing[7–9], chemical[8] and mechanical cleaning[10]. While annealing is considered to be the most effective method to "eliminate" the residues, a recent study casts doubts on the cleanliness of the processed graphene[11]. The characterization of graphene contaminants is of importance for the development of fabrication techniques for graphene-based devices.

To date, atomic force microscopy (AFM) and scanning tunnelling microscopy (STM) have been widely employed to study the surface of graphene and to characterize the extent of the residual contamination[7,8]. AFM can effectively reveal the morphology and concentration of a 2 nm thick residue film and STM can determine the effect of contaminants at the atomic scale. Both techniques suffer from a very low throughput and difficulties in the interpretation of results. Given the vast diversity of geometries and fabrication methods for graphene-based devices, AFM and STM may not be suitable for the imaging of a graphene surface in many cases, especially those involved in large-volume fabrication. Analytical techniques such as Raman spectroscopy[12], X-ray photoelectron spectroscopy[9,11] and terahertz emission spectroscopy[13] have served to characterize the changes in graphene's properties induced by contaminants. These techniques have a high throughput, however their application will be limited by their spatial resolution and the ability to determine the nature of the contamination. A rapid and effective method is required to study graphene cleanliness as well as determine the effectiveness of any actions taken to clean the graphene surface.

Secondary electron (SE) imaging in the scanning electron microscope (SEM) is an established characterization method for surface morphology, which is superior to AFM and STM in terms of image acquisition time,

magnification range, and image interpretation. In a SEM, SEs are excited by the irradiation of an energetic electron beam and collected from an image which reveals the morphology of the sample surface. Similarly, the relatively new helium ion microscope (HIM) utilizes a helium ion beam to excite SEs[14,15]. It has been demonstrated that HIM imaging is more surface sensitive with better spatial resolution, compared to SEM[16]. Both SEM and HIM have been employed to reveal the geometry of graphene nanostructures[1] and SE contrast in the SE images of graphene has been related to sample roughness, thickness[17,18] and intrinsic doping[19]. The formation mechanism of the SE contrast is still subject to some debate[17,20]. Reliable image interpretation as well as methods for quantitative analysis needs to be firmly established.

In addition, the ability of SE imaging to identify residues and contaminants on a graphene surface is rarely explored. One of the major challenges in resolving organic residues on graphene is caused by the absence of materials contrast, since both the contaminants and the graphene are carbon-based materials. The topographic contrast due to the non-uniformity of the contaminants does exist, but the ultrathin nature of the sample leads to a small interaction volume and small SE intensity. Nevertheless, it is imperative to clarify these issues for the application of SE imaging in graphene characterization.

In this work, we used both HIM and SEM to image the freestanding graphene fabricated on a Si substrate. The nanoscale polymethyl methacrylate (PMMA) residues can be observed by SE imaging. The observed contrast and morphology varied with the beam condition (i.e. beam type and beam energy). We have proposed a model based on the stacking of PMMA nanoparticles to explain the contrast. The contrast variation has been discussed based on the beam-sample interaction and SE formation. The results establish a quantitative method to evaluate the fidelity of SE imaging and provide a highly efficient method to reveal PMMA residues on a graphene surface.

Results

Figure 1 shows low-magnification images of different regions of the graphene sample observed using HIM, SEM, AFM and an optical microscope. The optical image in Figure 1a reveals the 2.2 μm holes in the Si substrate but neither the graphene nor its surface contamination are visible in the optical image. The graphene could be clearly seen when imaging using SEM and HIM (e.g. Figure 1b and 1c respectively). The freestanding graphene across the substrate holes (marked 'G' in Figure 1) exhibits a distinct contrast with respect to the bare holes (marked 'H' in Figure 1). The contrast is evident from ruptured graphene that covers a fraction of a hole. The boundary of the ruptured graphene is still visible in the supported area if we track the boundary from the hole to the substrate region. This contrast (i.e. graphene vs. substrate) is most distinguishable in the HIM image (Figure 1c). As a comparison, an AFM phase image is shown in Figure 1d, which also demonstrates the empty substrate holes, ruptured graphene across the holes, and rugged graphene surface.

Figure 2a is a HIM image of freestanding graphene, with a 0.3 nm pixel size and a 400 nm field of view (FOV). A non-uniform contrast is evident in the image; as marked in Figure 2a, the typical contrast features include bright spots (~10 nm in diameter), less-bright clusters (several hundred nanometers) and relatively dark areas surrounding these clusters. The contrast inside the dark area is not uniform, and the darkest regions appear as dot-like features, as shown in the inset of Figure 2a. We measured the diameters of 20 such dark dots (the diameter is defined as the full-width at half maximum (FWHM), of the SE intensity peak in the line-scan profile across the dot centre, see the supplementary information and Figure S1). The average size of these dots, measured from the HIM image (Figure 2a), is 2.7 ± 0.4 nm. To evaluate the fidelity of the HIM imaging, we then investigate the SE imaging of the same graphene sample in the SEM.
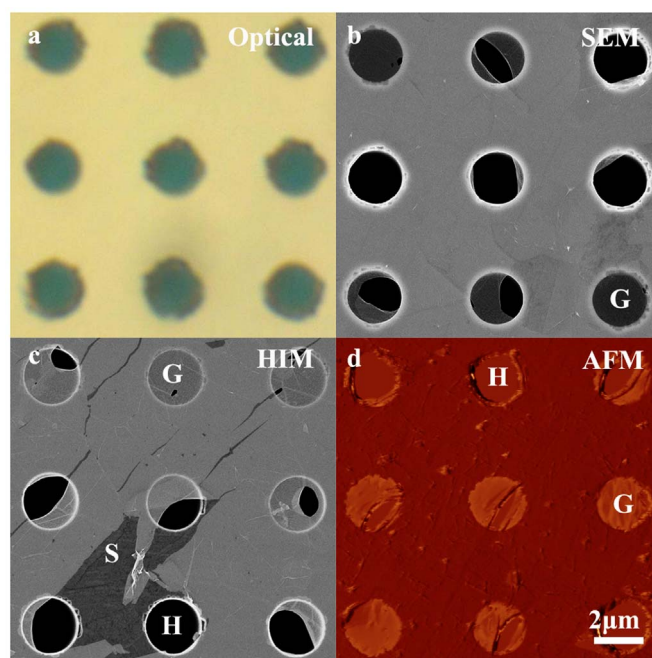

Figure 1 | **Low magnification images of the measured sample.** (a) An optical image of the graphene sample. Only the 3 × 3 hole arrays are shown on the Si substrate and no graphene contrast can be observed. (b) A 5 keV SEM image of the graphene sample. The existence of graphene (marked as 'G' in the image) can be identified from the substrate ('S') and the bare holes ('H'). (c) A 35 keV HIM image of the graphene sample. The image also shows the existence of graphene, substrate and bare holes. The graphene has a better contrast in HIM in comparison with SEM. (d) An AFM phase image of the graphene sample. Holes and freestanding graphene can be identified. The covering of graphene on the substrate is difficult to identify in the image at the selected magnification. All the images have the same field of view (2 μm scale bar shown in Figure 1a).

High-magnification SEM images (Figure 2b to 2d) were taken under e-beam energies of 0.5 keV, 10 keV and 20 keV, respectively. To facilitate the comparison, all the images in Figure 2, including the HIM image (Figure 2a), have a similar pixel size and same FOV, i.e. the same magnification. They show similar contrast features, and we can identify the bright spots, clusters and dark dots in the SEM images as well (see the inset of Figure 2b to 2d). We mention in passing that these contrast features can also be observed on the substrate-supported graphene in both SEM and HIM images (see the supplementary information). However, there are significant differences between these images (Figure 2). The lower the e-beam energy becomes, the higher the contrast exhibited in the corresponding image. That is to say, the typical features in the images (i.e. bright spots, clusters, and dark dots) have a larger difference in SE intensity at lower e-beam energies (see Figure 2b). To highlight the contrast variation, we plotted the histograms of the images as in Figure 2e. The most probable intensity for the 35 keV HIM image, i.e. the peak position in the histogram, is lower than the 20 keV SEM image, indicating that less SEs are escaping from the thick clusters in HIM. However, both the 35 keV HIM and the 20 keV SEM images demonstrate similarly symmetrical peaks in their image histograms. On the contrary, the histogram of the 0.5 keV SEM image exhibits an asymmetric peak, which is due to the existence of another peak at a high intensity value (indicated by the grey arrow).

Another significant difference among these images is the dimension of the dark dots. Although these dots are most discernable under the 0.5 keV e-beam imaging due to its high contrast, they have the largest apparent size of 7.2 ± 0.9 nm. As the electron beam energy increases, the size of the dark dots reduces. At the highest e-beam
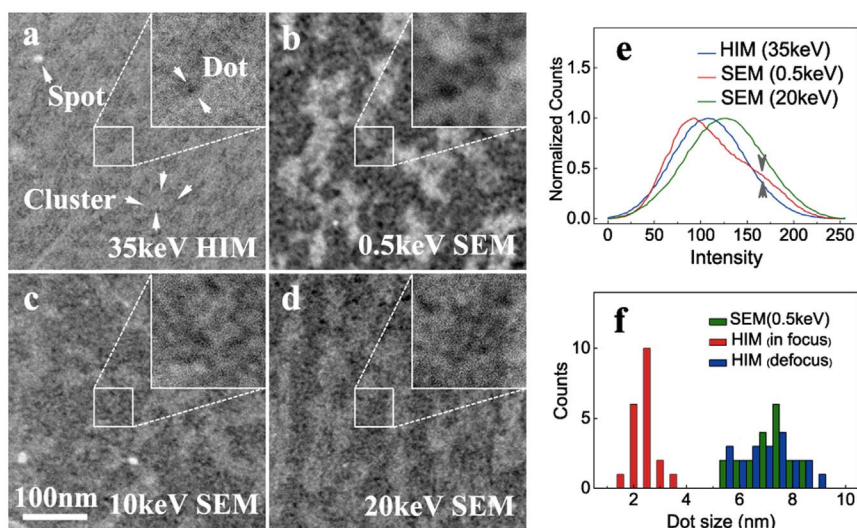
Figure 2 | High magnification SE images of freestanding graphene. (a) A 35 keV HIM image of the freestanding graphene. The featured structures such as bright spots, clusters and dark dots are marked by the arrows to show their existence. The dark dots can be observed more clearly from a selected and magnified area as shown in the white square frame. (b) A 0.5 keV SEM image of the freestanding graphene. (c) A 10 keV SEM image of the freestanding graphene. (d) A 20 keV SEM image of the freestanding graphene. The featured structures can also be observed in all these SEM images. All the SE images have the same FOV of 400 nm. (e) The intensity distributions for 35 keV HIM, 0.5 keV SEM and 20 keV SEM images. The 35 keV HIM and 20 keV SEM images exhibit similar and symmetric peaks. The peak of the 0.5 keV SEM image is asymmetric and has an additional peak at the high intensity value, as marked by the grey arrow. (f) The size distribution of the dark dots observed in the different imaging conditions. The dots observed in a finely focused 35 keV HIM image (Figure 2a) have small size values. The dots observed in a 0.5 keV SEM image (Figure 2b) and an over-focused 35 keV HIM image (Figure 3d) have similar size values due to their close probe size values.

energy that we used (20 keV), the average size of the dots decreases to 4.9 ± 0.7 nm, which is twice as large as that in the HIM images. As an example, the size distributions of the observed dark dots measured in the 0.5 keV SEM and 35 keV HIM are delineated in Figure 2f. It is evident that HIM gives a much narrower distribution and much smaller values for the measured sizes of the dark dots.

Discussion

Since the images taken at different beam conditions (beam species, beam energies, etc.) show distinct features, a valid question is which one of them exhibits the best fidelity to the graphene surface. To investigate the formation mechanisms of the SE contrast is thus of great importance to the interpretation of the images. It is well understood that the size of the beam probe is crucial to the resolution of the image[16]. The minimal probe size for a set of beam conditions is achieved when the probe is in focus and free of astigmatism (see the supplementary information for the optimization procedure to minimize the probe size). The images in Figure 2 were acquired with optimized probes, but the size of the smallest probe varied with the beam conditions. The electron probe size monotonously decreases from 2.7 ± 0.2 nm to 1.6 ± 0.1 nm as the e-beam energy increases from 0.5 keV to 20 keV, while in HIM the superlative probe size obtainable was 0.9 ± 0.1 nm (see Figure S5a in the supplementary information). The decrease of the beam probe size corresponds to improvement of spatial resolution. Therefore, the morphology difference observed in Figure 2 can be attributed to the variation of the probe size. As shown in Figure 3a, the size of the dark dots measured from a SEM image linearly depends on the size of the electron beam probe that was used to acquire the image. The linear relationship is valid for the e-beam energies that we tested (from 0.5 keV to 20 keV). A striking feature is that the He$^+$ probe fits the linear relationship as well. This can be demonstrated by tuning the He$^+$ beam into defocusing states and thus varying its probe size (see Figure S5b in the supplementary information). Figures 3b and 3c show the same area imaged by a focused He$^+$ beam (probe size $\sim$ 0.9 nm) first and then an over-focused beam (probe size $\sim$ 2.7 nm)

respectively. The featured structures such as bright spots, clusters and dots are still visible in the over-focused image. However, the average size of the dark dots in the over-focused image increases to 7.4 ± 1.2 nm, which is larger than the value (2.7 ± 0.4 nm) measured from the well-focused HIM image, but also quite close to the size (7.2 ± 0.9 nm) obtained from the 0.5 keV SEM image in Figure 2b. The distributions of the dot sizes in the over-focused HIM and 0.5 keV SEM images match well (see Figure 2f). The similarity of the two images can be inspected in Figures 3c and 3d, which is due to the fact that the size of the over-focused He$^+$ probe
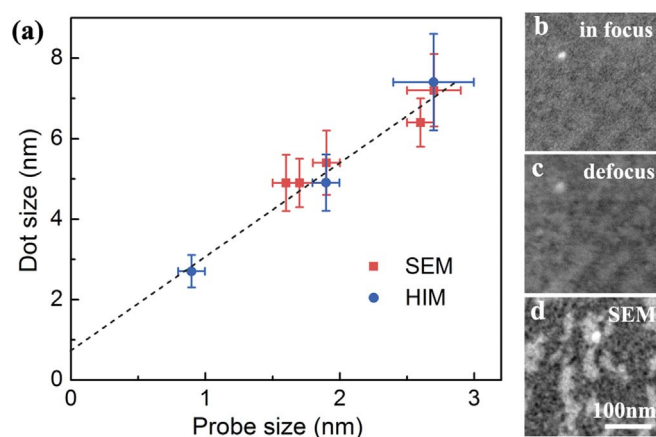

Figure 3 | Discussion of the similarities and differences between SEM and HIM images. (a) The relationship between the beam probe size and the dark dot size. A linear relationship (black dashed line) can be fitted for both the conditions of e-beam (red squares) and He$^+$ beam (blue circles). (b) A finely focused 35 keV HIM image of the freestanding graphene. The image shows a small dot size similar to Figure 2a. (c) A de-focused HIM image of Figure 3b. The observed dot size becomes larger than that of Figure 3b. (d) A finely focused 0.5 keV SEM image. The dot size is quite close to that of Figure 3c because of the close beam probe sizes for these two images.

(∼2.6 nm) is almost the same as that of the 0.5 keV SEM probe (∼2.7 nm). Therefore the correlation indicates that the measured size of the dark dots depends on the probe size and is independent of the beam type. The smaller the probe size becomes, the finer the dot which will be observed. We note that for all the imaging conditions, the probe size is smaller than the size of the dots in the corresponding image. However, the correlation of the probe size and the feature size indicates that the finite size of the probe may introduce errors to the measurement of feature dimension, even when the probe is smaller than the apparent size of the image feature. When the probe size decreases to zero, the apparent size of the feature will converge at the true feature size. As shown in Figure 3a, the y-intercept (0.7 ± 0.3 nm) corresponds to a zero-sized probe, and it might be the physical size of these dots, which is beyond the resolution limits of SEM and HIM. Nevertheless, compared with SEM, HIM imaging reveals the surface morphology with higher fidelity due to its finer probe. Besides the influence of beam probe size, the effects of beam-induced damage on the imaging fidelity need to be evaluated because both electron and helium ion beams are known to cause graphene damage[16,21]. However, for a dose up to 10^{17} cm^{-2}, the imaging fidelity is not affected by the damage (see Figures S6 to S9 in the supplementary information).

To understand the contrast mechanism of the SE imaging, we require knowledge of the graphene surface which should be acquired from other independent characterisation methods. Ishigami et.al. have exploited AFM and proved that a graphene surface –which has undergone a similar PMMA spin-coating process to our samples– will be covered by a continuous PMMA residue film[7]. Figure 4a is the high magnification AFM three-dimensional height image of our graphene film on the Si substrate. The featured structures observed in the SE imaging (Figure 2) appear in the AFM image, which can be directly interpreted as the surface roughness caused by the PMMA residues. Figure 4b shows the height variation across the bright spots in Figure 4a (A and B marked by the arrows). The height of the spots is about 4 nm. Since PMMA long chain molecules can form nanoparticles on the material surface with sizes of several nanometers[22,23], we postulate a model for the morphology of the graphene surface which is consistent with our AFM observation. As sketched in the inset of Figure 4a, the PMMA nanoparticles are assembled on the graphene surface to form a continuous but non-uniform film[23]. The in-plane close packing of the nanoparticles will form a uniform monolayer of residues. Regions of multi-layered PMMA residues are also present. The thickness of the monolayer PMMA is ∼4 nm, the same as the size of the nanoparticles. The AFM height profile shows that the multi-layered regions are normally thinner than ∼12 nm, i.e. less than three layers. The SE contrast (i.e. spots, clusters and dots) can be attributed to the non-uniform coverage of the residue layer. The formation of a SE image involves the propagation of the primary beam in the sample, the interaction between the primary particles and the sample atoms and the excitation and escape of the SEs. As shown in Figure 4c, the interaction range of the 0.5 keV e-beam in PMMA is ∼10 nm and a pear-like interaction volume extends across the top three PMMA layers. For the 20 keV e-beam, the interaction volume in the top three PMMA layers is a narrow cone (Figure 4c). To understand the significance of the geometry variation of the interaction volume, consider the interaction volume of the e-beam in the three layers of PMMA on the graphene surface at low energy (0.5 keV) (V_L) and for the high energy (20 keV) (V_H). Now we label the interaction volumes for just the top layer as V_H^T and V_L^T for the high and low energies respectively. Since the interaction volume of the high-energy beam approximates to a conical shape, the ratio of V_H^T/V_H is close to 0.03. As shown in Figure 4c, it is clear that the ratio of V_L^T/V_L is smaller than V_H^T/V_H due to the fact that the majority of the pear-like interaction volume situates in the second layer. We see that for a low energy beam a lower portion is lost in the top layer than the portion lost for a high energy
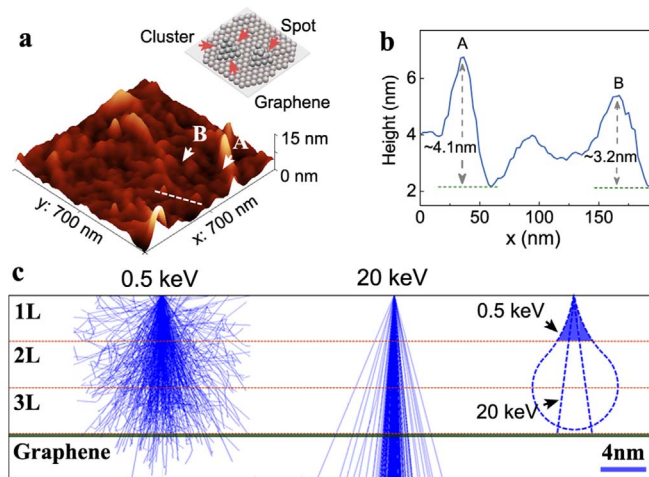

Figure 4 | The PMMA nanoparticle stacking model for the formation of surface roughness and dark dots. (a) The three-dimensional AFM height image of the substrate-supported graphene with a FOV of 700 nm. A white dashed line is drawn across two peaks (marked as A and B by the arrows) to show its height variation. Inset: A demonstration of the stacking model for the PMMA nanoparticles. PMMA nanoparticles can be stacked as monolayer or multilayers (clusters and dots) on the graphene surface. (b) The height profile of the dashed line in Figure 4a. Spots A and B are shown as two peaks that have large height intensities. (c) The simulated interaction volume of the electrons in the top three layers of PMMA on a graphene surface. The interaction volume of the 0.5 keV electrons in the region exhibits a pear-like shape, while the interaction volume of the 20 keV electrons is a narrow conical shape (see the dashed shapes in the figure). The volume ratio of the top PMMA layer to the total PMMA layers is smaller for the interaction with the 0.5 keV electrons than the 20 keV electrons.

beam. For the low energy beam, this results in a larger intensity difference across regions with different thicknesses. This is responsible for the increased contrast and contributes to the larger probe size found at the lower beam energy. On the other hand, the higher the electron beam energy is, the lower the scattering cross section between the energetic electrons and the material electrons. This effect results in the translucent appearance of the sample at higher beam energies. This translucency is not apparent in the HIM imaging. This is due to the stopping power of the 35 keV He$^+$ beam and the electron beam's different interaction behaviour with carbon. As the He$^+$ beam propagates through the sample, it continues losing energy. The lower the beam energy, the lower the stopping power, and thus the lower excitation of secondary electrons. This means that the majority of the SEs collected in the HIM is from the top layer, resulting in high surface sensitivity of the HIM imaging. The stopping power of the electron beam behaves in an opposite way, which enhance the SE emission from the underlying layers and thus enhances the translucency of the sample. To summarize, the nanoparticles identified in the AFM height profile (Figure 4a) correspond to the brightest spots in the SE images (Figure 2a). The darkest dots in the SE images indicate areas of the sample surface that might not be covered by the residue PMMA, i.e. the interstice of the PMMA nanoparticles. The close stacking of spherical nanoparticles with a diameter of ∼4 nm will result in an interstice of ∼0.6 nm, which coincides with the size of the dark spots extrapolated for a zero-sized probe.

Besides the residues on the graphene surface, the SE imaging reveals abundant surface information, for example, the multilayer folds, ridges and the surface ruggedness (Figure 5), while the detailed contrast of these features, i.e. their apparent morphology in the images, depends on the imaging conditions as well. For example, as shown in Figure 5a, in the HIM image the folds of graphene are
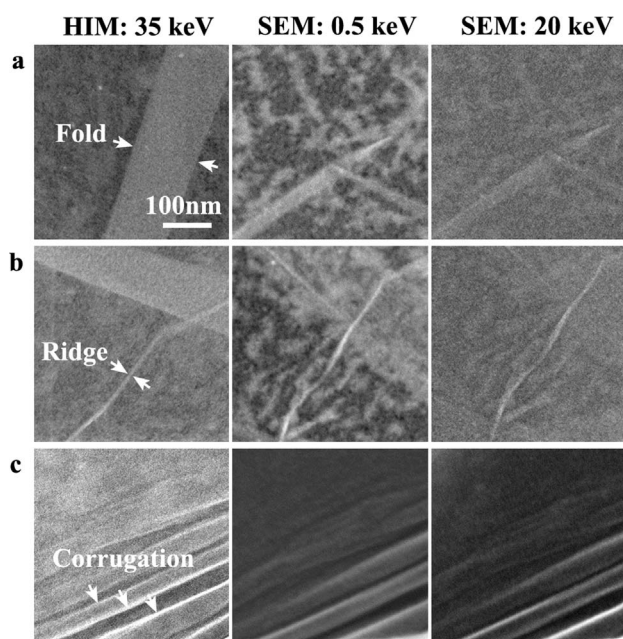
Figure 5 | Comparison of other graphene surface features. (a) The observation of the graphene folds in different microscopes. Graphene folds show different contrast in the 35 keV HIM, 0.5 keV SEM and 20 keV SEM images. (b) The observation of the graphene ridges in different microscopes. (c) The observation of graphene corrugations in different microscopes.

portrayed as regions of uniform brightness –in contrast to the darker graphene background– with clearly defined straight edges. The folds observed in the 0.5 keV SEM image are similar to those in the HIM; however in the 20 keV SEM image their contrast significantly decreases due to the increase of sample translucency. Figures 5b and 5c are topographical features of the graphene (ridges and corrugation), which demonstrate the high surface sensitivity of HIM imaging.

In conclusion, we have demonstrated the visibility of nanoscale PMMA residues on a graphene surface in secondary electron imaging. Artefacts have been attributed to the finite probe size and the varying nature of the beam-sample interaction at different beam conditions. In terms of imaging fidelity, HIM is superior to SEM, since HIM provides a sub-nanometer probe and increases surface sensitivity. The low-energy SEM images however demonstrate higher contrast. Other features such as folds, ridges and ruggedness could also be observed in the SE imaging. The results establish a quantitative method to evaluate the fidelity of SE imaging and provide a high efficiency method to reveal the PMMA residues on a graphene surface.

Methods

Graphene synthesis and transfer. The continuous monolayer graphene was grown on the 25 μm thick Cu foils (Alfa Aesar, 99.8% purity) by the chemical vapour deposition process reported previously[24]. A thin PMMA layer (Molecular weight = 950 k a.m.u) was spin-coated on the graphene/Cu foil, followed by the etching of Cu foil in an aqueous iron(III) chloride solution. The remaining PMMA/graphene film was rinsed in deionized water three times and then transferred onto the target Si substrate. The substrate contained arrays of circular holes of ~2.2 μm in diameter and 5 μm in depth, which was fabricated by photolithography patterning followed by inductively coupled plasma (ICP) reactive-ion etching (RIE). The PMMA layer was dissolved in 55°C hot acetone for 15 minutes first, then transferred to 55°C hot IPA for 15 minutes, slowly taken out of the solvent and then dried in ambient conditions.

Characterization of graphene surface morphology. The imaging of the fabricated graphene sample was carried out in both a helium ion microscope and scanning electron microscope. The SEs in HIM (Zeiss Orion Plus) were excited by a focused He$^+$ beam of 35 keV beam energy and 0.6 pA beam current (10 μm aperture), and collected by an Everhart-Thornley detector. While the SEs in SEM (Zeiss Supra) were

excited by the beam energy from 0.5 keV to 20 keV and collected by an in-lens detector. The beam current increased from 10 pA to 35 pA. To minimize the influence of possible beam induced contamination, the selected region was only scanned once. All the captured SE images were transformed so that the intensity histogram was extended to the whole 0–255 region. The morphology of graphene was also characterized by optical microscopy (Olympus BX51, 50× objective lens) and atomic force microscopy (Asylum MFP-3D, tapping mode with tip diameter < 20 nm).

Simulation of beam interaction volume. The simulation was carried out using Casino (v2.48). The substrate material was defined as PMMA (composition $C_5O_2H_8$). Two beam energies of 0.5 keV and 20 keV were selected, 20000 electrons were used to simulate the distribution. Figures 4d and 4e show the distribution of 500 simulated electrons.

1. Novoselov, K. S. *et al.* Electric field effect in atomically thin carbon films. *Science* **306**, 666–669 (2004).
2. Castro Neto, A. H., Guinea, F., Peres, N. M. R., Novoselov, K. S. & Geim, A. K. The electronic properties of graphene. *Rev. Mod. Phys.* **81**, 109–162 (2009).
3. Geim, A. K. & Novoselov, K. S. The rise of graphene. *Nat. Mater.* **6**, 183–191 (2007).
4. Ju, L. *et al.* Graphene plasmonics for tunable terahertz metamaterials. *Nat. Nano.* **6**, 630–634 (2011).
5. Fan, J. *et al.* Investigation of the influence on graphene by using electron-beam and photo-lithography. *Solid State Commun.* **151**, 1574–1578 (2011).
6. Novoselov, K. S. *et al.* A roadmap for graphene. *Nature* **490**, 192–200 (2012).
7. Ishigami, M., Chen, J. H., Cullen, W. G., Fuhrer, M. S. & Williams, E. D. Atomic structure of graphene on SiO$_2$. *Nano Lett.* **7**, 1643–1648 (2007).
8. Cheng, Z. *et al.* Toward intrinsic graphene surfaces: a systematic study on thermal annealing and wet-chemical treatment of SiO$_2$-supported graphene devices. *Nano Lett.* **11**, 767–771 (2011).
9. Pirkle, A. *et al.* The effect of chemical residues on the physical and electrical properties of chemical vapor deposited graphene transferred to SiO$_2$. *Appl. Phys. Lett.* **99**, 122108 (2011).
10. Goossens, A. M. *et al.* Mechanical cleaning of graphene. *Appl. Phys. Lett.* **100**, 073110 (2012).
11. Lin, Y.-C. *et al.* Graphene annealing: how clean can it be? *Nano Lett.* **12**, 414–419 (2011).
12. Yu, G. *et al.* Spatially-resolved ultrafast optical spectroscopy of polymer-grafted residues on CVD graphene. *J. Phys. Chem. C* **118**, 708–713 (2013).
13. Sano, Y. *et al.* Imaging molecular adsorption and desorption dynamics on graphene using terahertz emission spectroscopy. *Sci. Rep.* **4** (2014).
14. Pearson, A. J., Boden, S. A., Bagnall, D. M., Lidzey, D. G. & Rodenburg, C. Imaging the bulk nanoscale morphology of organic solar cell blends using helium ion microscopy. *Nano Lett.* **11**, 4275–4281 (2011).
15. Rodenburg, C., Viswanathan, P., Jepson, M. A. E., Liu, X. & Battaglia, G. Helium ion microscopy based wall thickness and surface roughness analysis of polymer foams obtained from high internal phase emulsion. *Ultramicroscopy* **139**, 13–19 (2014).
16. Fox, D. *et al.* Helium ion microscopy of graphene: beam damage, image quality and edge contrast. *Nanotechnology* **24**, 335702 (2013).
17. Kochat, V. *et al.* High contrast imaging and thickness determination of graphene with in-column secondary electron microscopy. *J. Appl. Phys.* **110**, 014315 (2011).
18. Guo, H., Gao, J., Ishida, N., Xu, M. & Fujita, D. Characterization of two-dimensional hexagonal boron nitride using scanning electron and scanning helium ion microscopy. *Appl. Phys. Lett.* **104**, 031607 (2014).
19. Yan, K. *et al.* Modulation-doped growth of mosaic graphene with single-crystalline p–n junctions for efficient photocurrent generation. *Nat. Commun.* **3**, 1280 (2012).
20. Cazaux, J. Calculated dependence of few-layer graphene on secondary electron emissions from SiC. *Appl. Phys. Lett.* **98**, 013109 (2011).
21. Teweldebrhan, D. & Balandin, A. A. Modification of graphene properties due to electron-beam irradiation. *Appl. Phys. Lett.* **94**, 013101 (2009).
22. Peterson, K. A., Zimmt, M. B., Linse, S., Domingue, R. P. & Fayer, M. D. Quantitative determination of the radius of gyration of poly(methyl methacrylate) in the amorphous solid state by time-resolved fluorescence depolarization measurements of excitation transport. *Macromolecules* **20**, 168–175 (1987).
23. Peng, B., van der Wee, E., Imhof, A. & van Blaaderen, A. Synthesis of monodisperse, highly cross-linked, fluorescent PMMA particles by dispersion polymerization. *Langmuir* **28**, 6776–6785 (2012).
24. Li, X. *et al.* Large-area synthesis of high-quality and uniform graphene films on copper foils. *Science* **324**, 1312–1314 (2009).

Author contributions

Y.Z. prepared the graphene sample. Y.Z., R.O.C. and H.Z. designed and conducted the experiment. H.Z. supervised the project and led the overall effort. Y.Z., R.O.C., P.M. and H.Z. contributed to data analysis and writing of the manuscript at all stages.

Additional information

Supplementary information accompanies this paper at http://www.nature.com/scientificreports

Competing financial interests: The authors declare no competing financial interests.

How to cite this article: Zhou, Y., O'Connell, R., Maguire, P. & Zhang, H. High throughput secondary electron imaging of organic residues on a graphene surface. *Sci. Rep.* **4**, 7032; DOI:10.1038/srep07032 (2014).